Coupled Flow and Geomechanical Analysis for Gas Production in the Prudhoe Bay Unit L-106 Well Unit C Gas Hydrate Deposit in Alaska

Jihoon Kim[a], George J. Moridis[a], Jonny Rutqvist[a]

[a]*Earth Sciences Division, Lawrence Berkeley National Laboratory. 1 Cyclotron Road 90R1116, Berkeley, CA 94720, USA*

Abstract

We perform numerical simulation for the gas hydrate reservoir, in the vicinity of Prudhoe Bay Unit L-Pad on the North Slope (i.e., Unit C in the PBU-L 106 site), considering vertical and horizontal well production scenarios. In order to analyze coupled flow and geomechanics more rigorously we employ two-way coupling between fluid flow and geomechanics, and compare the results with those from one-way coupling used in previous studies, where two-way coupling accounts for changes in pore volume induced by geomechanics, while one-way coupling does not. We find clear differences in the variables of flow and geomechanics between one-way and two-way couplings in this field case (e.g., pressure and effective stress). Using geomechanical properties used previously for the PBU-L 106 C unit, we find that the effective stresses are within the elastic region, located away from the Mohr-Coulomb yield function for both vertical and horizontal well production scenarios. This implies that we face little danger in geomechanical instability and failure. We also investigate vertical displacement to assess well stability, using two-way coupling. The results from the vertical well scenario show small vertical displacement, from which we anticipate that the vertical well will be stable and safe. On the other hand, the horizontal well scenario causes larger subsidence for a given simulation time because of higher production rates. Even in the case that the hydrates are completely dissociated and the aqueous phase pressure is equilibrated with the constant bottom hole pressure, the estimates of the maximum vertical displacement and strain are 73 cm and 2%, respectively, which do not appear to be a danger of potential well failure. Based on the results and analyses, the horizontal well production is feasible for gas production from the hydrate layers of Unit C in the PBU-L 106 site. But the reservoir model used in this study is relatively generalized. Thus, a specific reservoir model for the site will be required for higher accuracy in the future, after we obtain accurately measured geomechanical data and failure models.

Email addresses: JihoonKim@lbl.gov (Jihoon Kim), GJMoridis@lbl.gov (George J. Moridis), JRutqvist@lbl.gov (Jonny Rutqvist)

Keywords: Hydrate deposits, Poromechanics, Geological stability, Wellbore stability, Geomechanics, Gas hydrates.

1. Introduction

1.1. Background and motivation.

Gas hydrate reservoirs are considered as one of the potentially substantial future energy resources because of its abundance and the rapidly increasing global energy demand (Collett et al., AAPG Memoir 2009). Although there is no accurate current estimate of the gas hydrate volumes, which widely range between 10^{15} and 10^{18} m^3 (Milkov, 2005; Klauda and Sandler, 2005; Sloan and Koh, 2008; Collett et al., AAPG Memoir 2009), the quantity is known to be enormous. As an example of a conservative estimate, according to Milkov (2005), $(1-5) \times 10^{15}$ m^3 is the estimate that best reflects the current knowledge of submarine gas hydrate.

Gas hydrates are solid crystalline compounds of water and gas molecules trapped within the lattice of ice crystals (Sloan and Koh, 2008). Trapped gases and the ice crystals are called *guests* and *hosts*, respectively. The formation and dissociation of the hydrates are expressed, according to the exothermic equation, as

$$G + N_H \; H_2O = G \cdot N_H \; H_2O + Q_H, \tag{1}$$

where $G \cdot N_H H_2O$ is the hydrate, G denotes a hydrate-forming gas, N_H is the corresponding hydration number, and Q_H is the specific enthalpy of hydrate formation/dissociation. CH_4, methane, takes the majority of the gaseous components, although natural hydrates can include several guests such as CH_4, CO_2, H_2S, and N_2. CH_4 is concentrated up to a factor of 164, when compared to standard pressure and temperature conditions (Moridis, 2003).

Hydrates are generally encountered in two distinctly different geologic settings where the conditions of low temperature T and high pressure P that favor their formation and stability are satisfied: in the Arctic and in the oceans. The three main hydrate dissociation methods (Makogon, 1987, 1997) that can be used for hydrocarbon recovery (Moridis et al., 2009) are as follows.

- Depressurization, which occurs when pressure is lowered below the pressure of hydrate stability at a given temperature.
- Thermal stimulation, which involves raising temperature above the dissociation temperature for a given pressure.

- Inhibitor effects, involving the use of substances such as brines and alcohols that destabilize the hydrates.
- Chemical exchange utilizing CO_2 that can replace CH_4.

When CH_4 is produced from hydrate reservoirs, flow is tightly coupled to geomechanics because changes in fluid pressure and temperature highly affect effective stress in geomechanics (Kim et al., 2012; Rutqvist and Moridis, 2009; Rutqvist et al., 2009). Hydrate deposits that are desirable gas production targets almost invariably involve coarse, unlithified, unconsolidated media (such as sands and gravels). According to Rutqvist and Moridis (2009) and Rutqvist et al. (2009), hydrate dissociation can induce weak mechanical strength of the gas hydrate porous media and significant deformations of the hydrate deposits. The deformations cause changes in pore volume and permeability, resulting in redistributions of pore pressure and saturation, immediately, because the geomechanical changes propagate from the well toward the boundaries instantaneously because of the nature of the quasi-static mechanics (Kim et al., 2012).

Even though fluid flow and geomechanics need to be considered as coupled processes in order to accurately predict the reservoir behavior during gas production from hydrates, such coupling has received limited attention. In previous studies on gas hydrate reservoirs, Rutqvist et al. (2011) performed geomechanical analyses on potential future long-term tests of gas production from hydrate deposits at Mount Elbert (Unit D) and Prudhoe Bay L-Pad vicinity in North Slope (Unit C in the PBU-L 106 site), Alaska. In the analyses, the horizontal production well was used for the D-unit, whereas the vertical production well was used for the C-unit. The results of Rutqvist et al. (2011) show larger subsidence around the well in Unit C at the PBU-L 106 site than Unit D in Mount Elbert, although both of them indicate no significant interference with nearby wells in geological stability. But Rutqvist et al. (2011) limited their analyses to one-way coupling, considering the effect from fluid flow to geomechanics only, but not the other way around. Moridis et al. (2010) investigated gas production in vertical and horizontal wells in the PBU-L 106 C unit, comparing them with the PBU-L 106 D unit. The results show that the horizontal well in the PBU-L 106 C unit can increase gas production, compared with other cases. However, the results are obtained simply by using a pore-compressibility, not considering coupled flow and geomechancis. Thus more rigorous geomechanical analyses are required for highly accurate prediction of the hydrate reservoir behavior, for example, using two way coupling between fluid flow and geoemechanics.

1.2. Objectives and approaches.

With the aforementioned motivation, we perform analyses on coupled flow and geomechanics for both vertical and horizontal production wells in Unit C in the Prudhoe Bay Unit L-Pad site (i.e., PBU-L 106 C unit). In this paper, we employ two-way coupling between fluid flow and geomechanics in order to predict behavior of hydrate reservoirs in the C-unit more accurately (e.g., geological stability and subsidence), and compare the results with those from the one-way coupling method. In contrast with one-way coupling, by two-way coupling we consider not only the effects from pore pressure of fluid flow to geomechanics but also changes from geomechanics to pore volume of flow.

According to Kim et al. (2012), we anticipate significant differences between one-way and two-way couplings for coupled fluid flow and geomechanics in the case of high coupling strength (i.e., incompressible fluid such as water), where the coupling strength between geomechanics and fluid flow is given by the ratio of the bulk stiffness of the fluid to that of the solid skeleton (Kim et al., 2011a), different time scale between fluid flow and geomechanics, and low pressure diffusion (i.e., early time or low permeability), which fall in most hydrate reservoirs. From these reasons, we employ two-way coupling between fluid flow and geomechanics for hydrate reservoirs in this paper, while still using one-way coupling from heat flow to geomechanics. One-way coupling between heat flow and geomechanics can be valid in the case of large heat capacity or small heat contribution from deformation of reservoirs (Lewis and Schrefler, 1998).

Thus, we apply the two-way coupling method to a field case study of Unit C in the PBU-L 106 site in this paper. There are two solution schemes to simulate coupled flow and geomechanics: fully coupled (monolithic) and sequential approaches. The fully coupled methods require a unified flow-mechanics simulator and considerable computational cost, although they provide numerical unconditional stability (Lewis and Sukirman, 1993; Gutierrez and Lewis, 2002; Lewis et al., 2003; Jean et al., 2007). On the other hand, sequential schemes can make use of existing robust simulators by constructing an interface between flow and mechanics simulators (Settari and Mourits, 1998; Armero, 1999; Kim et al., 2011a). However, in general, sequential schemes do not guarantee numerical unconditional stability, and significant efforts have been made to find a reliable sequential method that can be competitive in terms of accuracy with the corresponding fully coupled method. Recently, from Kim et al. (2011b) and Kim et al. (2011c), the fixed-stress split is a highly recommended sequential method because it provides unconditional stability and high accuracy, as well as efficiency in implementing the interface code. The *fixed-stress split* method involves first the solution of the coupled problem of fluid flow

and heat transport (while keeping the total stress fields frozen, but allowing the strain fields to vary) to estimate pressure, temperature, and saturation, followed by the solution of the geomechanical equations to estimate the displacements.

We employ the fixed-stress split as a reliable sequential method, making use of existing robust simulators (i.e., TOUGH+HYDRATE for flow and FLAC3D for geomechanics) (Kim et al., 2012). We employ a relatively generalized reservoir model, which is the same as that of Moridis et al. (2010) in order to predict the general behavior of the PBU-L 106 C unit. From numerical simulations in the vertical and horizontal wells in the PBU-L 106 C unit, we find noticeable differences in aqueous pressure and effective stress between the one-way and two-coupling methods. We also perform analyses on geological stability for the vertical and horizontal wells. During simulation the effective stresses defined for the Mohr-Coulomb failure condition are still within the elastic region for both vertical and horizontal production well scenarios. This implies that we can predict little danger in geological instability. As for wellbore stability, the horizontal well production causes larger subsidence for a given simulation time because of higher production rates than the vertical well production. However, the estimates of the maximum vertical displacement and strain do not appear to be a danger of potential well failure, and thus the horizontal well production is feasible for gas production.

2. Unit C in the PBU-L 106 site

The PBU-L-106 site is located on the North Slope of Alaska (Moridis et al., 2010; Collett, 2007), as shown in Figure 1. The geology and petroleum geochemistry of the gas hydrate deposits in North Slope of Alaska have been studied and described (e.g., Bird and Magoon (1987) and Collett (1993)). The gas hydrate on the North Slope was in 1972 confirmed directly by the data from the Northwest Eileen State-2 well, located in the northwest part of the Prudhoe Bay area (Figure 1) (e.g., Collett et al. (2011)). Then, the data of the additional 50 exploratory and production wells were obtained, and the existence of six hydrate layers (A, B, C, D, E, F units) was identified, as shown in Figures 1 and 2. Units A, B, C, D are interpreted to hold large volumes of free gas down-dip (Collett, 2007).

Unit C in the PBU-L 106 site consists of two separate hydrate-bearing units: Based on the well logging data, C1 (deeper) and C2 (shallower) (Collett, 1993; Moridis et al., 2010; Collett et al., AAPG Memoir 2009), as shown in Figure 2. Unit C ranges from 678.5 m to 723.6 m in depth. The thickness of C1 and C2 is 18.9 m and 17.1 m, respectively. There is one shale interlayer between C1 and C2, thickness of which is 9.2 m. Unit

C has impermeable boundaries at top and bottom (i.e., Class 3 hydrate deposit) (Moridis, 2003; Moridis et al., 2010). The hydrate layers have high intrinsic permeability ($1 - 5$ Darcy, where 1 Darcy $= 9.87 \times 10^{-13}\ m^2$), high porosity (0.4), and high hydrate saturation (0.75). The hydraulic pressure is distributed from 7.3 MPa (top) to 7.7 MPa (bottom). The temperature ranges from 5^oC to 6.5^oC.

We use flow and geomechanical properties of Unit C in Mount Elbert for simulation of Unit C in the PBU-L 106 site, because the two units are stratigraphically correlative (Collett et al., 2011). The drained bulk and shear moduli are 95 MPa and 87 MPa for zero solid saturation (i.e., ice plus hydrate saturation), respectively, while drained bulk and shear moduli are 670 MPa and 612 MPa for full solid saturation, respectively. There are several experiments to estimate geomechanical properties for gas hydrate bearing sediments (Masui et al., 2005, 2008; Miyazaki et al., 2010c,a,b). The experiments and their estimates are based on Toyoura sand, which consists of silicon dioxide SO_2 as a major component. The geomechanical properties of the Mallik samples are similar to those of Toyoura Sand (Winters et al., 1999, 2008). Then, from the results of Masui et al. (2005) and Masui et al. (2008), Rutqvist et al. (2009) used a linear relation between the drained shear/bulk moduli and hydrate saturation for numerical simulation of hydrate deposits in Mallik (Canada) and Mount Elbert (Alaska, U.S.), as shown in Figure 3.

For plasticity, according to results of Miyazaki et al. (2010b), the shear strength for the Mohr-Coulomb plastic model is a function of the effective confining volumetric (mean) stress and hydrate saturation. The cohesion increases with the hydrate saturation, but the friction angle is almost independent of the hydrate saturation (Miyazaki et al., 2010c,a,b). Considering those experimental results, Rutqvist and Moridis (2009) and Rutqvist et al. (2009) used a linear relation between the hydrate saturation and cohesion for numerical simulation. They used the Mohr-Coulomb failure model, which can implicitly account for dependency on the confining volumetric (mean) stress. The cohesion of the Mohr-Coulomb model is 0.5 MPa for zero solid saturation and 2.0 MPa for full solid saturation. The friction and dilation angles are 30 and 10 degrees, respectively. In this paper, we follow Rutqvist and Moridis (2009) and Rutqvist et al. (2009)'s approximation for geomechanical elastic and plastic properties.

3. Numerical approach

3.1. Governing equations for flow and geomechanics

We restate the governing equations for coupled fluid/heat flow and geomechanics described in Kim et al. (2012). The governing equation for fluid flow comes from mass balance, written as,

$$\frac{d}{dt}\int_\Omega m^k d\Omega + \int_\Gamma \mathbf{f}^k \cdot \mathbf{n} d\Gamma = \int_\Omega q^k d\Omega, \tag{2}$$

where the superscript k indicates the fluid component. m^k, $\mathbf{f}^k$, and q^k are mass of the component k, and its flux and source terms on the domain Ω with the boundary Γ, respectively. We denote by $d(\cdot)/dt$ the time derivative of a physical quantity $(\cdot)$ relative to the motion of the solid skeleton. In long-term gas production from hydrates, Kowalsky and Moridis (2007) showed that dissociation can be accurately described as an equilibrium (as opposed to kinetic) reaction. Under these conditions, only two components need be considered: H_2O ($\kappa = w$) and CH_4 ($\kappa = m$), i.e., hydrate is considered as just one possible state of the CH_4-H_2O system. These two components are distributed among four possible phases J, i.e., aqueous ($J = A$), gaseous ($J = G$), hydrate ($J = H$), and ice ($J = I$). Then, the accumulation term m^κ ($\kappa \equiv w, m$) is given by

$$m^k = \sum_{J=A,G,H,I} \phi\, S_J\, \rho_J\, X_J^k, \quad k \equiv w, m \tag{3}$$

where ϕ is the true porosity, defined as the ratio of the pore volume to the bulk volume in the deformed configuration; S_J and ρ_J are saturation and density of the phase J, respectively; and X_J^k is the mass fraction of component k in the phase J. Obviously, $X_I^w = 1$. From the hydrate stoichiometry, $X_H^w = N_H W^w/(W^m + N_H W^w)$ and $X_H^m = 1 - X_H^w$, where W^m and W^w are the molecular weights of CH_4 and H_2O, respectively.

The mass flux term $\mathbf{f}^k$ in Equation 2 is given by

$$\mathbf{f}^k = \sum_{J=A,G} \left(\mathbf{w}_J^k + \mathbf{J}_J^k\right), \tag{4}$$

where $\mathbf{w}_J^k$ and $\mathbf{J}_J^k$ are the convective and diffusive mass flows of component k in the phase J. The summation over the phases J is limited to the mobile A and G, the solid phases H and I being immobile. For the aqueous phase, $\mathbf{w}_A^k$ is described by Darcy's law as

$$\mathbf{w}_A^k = X_A^k\, \mathbf{w}_A, \quad \mathbf{w}_A = -\frac{\rho_A\, k_{rA}}{\mu_A}\, \mathbf{k}\, (\mathbf{Grad} P_A - \rho_A\, \boldsymbol{g}), \tag{5}$$

where $\mathbf{k}$ is the absolute permeability tensor; μ_J, k_{rJ}, and P_J are the viscosity, relative permeability, and pressure of the fluid phase J, respectively. $\boldsymbol{g}$ is the gravity vector, and $\mathbf{Grad}$ is the gradient operator. For the gaseous phase, $\mathbf{w}_G^k$ can be written as

$$\mathbf{X}_G^k = X_G^k \, \mathbf{w}_G, \quad \mathbf{w}_G = -\left(1 + \frac{k_K}{P_G}\right) \mathbf{k} \, \frac{\rho_G \, k_{rG}}{\mu_G} \, (\mathbf{Grad} P_G - \rho_G \, \boldsymbol{g}), \tag{6}$$

where k_K is the Klinkenberg factor. The diffusive flow $\mathbf{J}_J^k$ ($k \equiv m, w; J \equiv A, G$) is described as

$$\mathbf{J}_J^J = -\phi \, S^J \, \tau_G \, \mathbf{D}_J^k \, \rho_J \, \mathbf{Grad} X_J^k, \tag{7}$$

where $\mathbf{D}_J^k$ is the hydrodynamic dispersion tensor, and τ_G is the gas tortuosity, often computed from the Millington and Quirk (1961) model as $\tau_G = \phi^{1/3} S_G^{7/3}$.

According to Equation 1, the dissociation/formation of methane hydrates are described as

$$CH_4 \cdot N_H H_2O \, (\text{hydrate}) \leftrightarrow CH_4(\text{gas}) + N_H H_2O + Q_H \, (\text{liquid or ice}), \tag{8}$$

where N_H is the hydration number specific to the methane hydrate. The reaction of Equation 8 is depicted on the phase diagram of the water- methane- vapor(gas)-hydrate system, shown in Figure 4, as the 3-phase co-existence lines of A+G+H (when liquid water is involved) and I+G+H (when ice is involved), and includes the quadruple point Q_1.

The governing equation for heat flow comes from energy balance, written as,

$$\frac{d}{dt} \int_\Omega m^\theta d\Omega + \int_\Gamma \mathbf{f}^\theta \cdot \mathbf{n} d\Gamma = \int_\Omega q^\theta d\Omega, \tag{9}$$

where the superscript θ indicates the heat component. m^θ, $\mathbf{f}^\theta$, and q^θ are heat, its flux, and source terms on the domain Ω with the boundary Γ, respectively. The heat accumulation term m^θ becomes

$$m^\theta = (1 - \phi) \int_{T_0}^{T} \rho_R \, C_R \, dT \; + \sum_{J=A,G,H,I} \phi \, S_J \, \rho_J e_J, \tag{10}$$

where $\rho_R = \rho_R(T)$ and $C_R = C_R(T)$ are the density and heat capacity of the porous medium, respectively; T is the temperature; T_0 is a reference temperature; and e_J is the specific internal energy of phase J. The heat flow $\mathbf{f}^\theta$ includes conduction and convection contributions, and is described as

$$\mathbf{f}^{\theta} = -\mathbf{K}_{\theta}\nabla T + \sum_{J=A,G} h_J \, \mathbf{w}_J, \tag{11}$$

where $\mathbf{K}_{\theta}$ is the composite thermal conductivity of the porous media and phase J system, and h_J is the specific enthalpy of phase J. e_J and h_J are given by

$$e_J = \sum_{k=w,m} X_J^k \, e_J^k \quad \text{and} \quad h_J = \sum_{k=w,m} X_J^k \, h_J^k, \tag{12}$$

where e_J^k and h_J^k indicate the specific internal energies and enthalpies of components k in the phase J. Note that, under equilibrium conditions, the heat of hydrate dissociation is accounted for when differencing the hydrate mass between two points in time, i.e.,

$$\Delta m^{\theta} = (1-\phi)\int_{T_1}^{T_2} \rho_R \, C_R \, dT \; + \Delta(\sum_{J=A,G,I} \phi \, S_J \, \rho_J \, e_J) + H_D \, \Delta(\phi \, S_H \, \rho_H), \tag{13}$$

where T_1 and T_2 are the temperatures at these two times, and H_D is the heat of hydrate dissociation.

The governing equation for geomechanics based on the quasi-static assumption is written as

$$\mathrm{Div}\,\boldsymbol{\sigma} + \rho_b \boldsymbol{g} = \mathbf{0}, \tag{14}$$

where $\mathrm{Div}(\cdot)$ is the divergence operator, $\boldsymbol{\sigma}$ is the Cauchy total-stress tensor. ρ_b is the bulk density. We adopt a continuum theory in coupled flow and geomechanics, where the fluid and solid are considered as overlapping continua. Note that tensile stress and strain are positive. For elastoplasticity, we employ the Mohr-Coulomb model, written as

$$f = \tau'_m - \sigma'_m \sin\Psi_f - c_h \cos\Psi_f \leq 0, \tag{15}$$

$$g = \tau'_m - \sigma'_m \sin\Psi_d - c_h \cos\Psi_d \leq 0, \tag{16}$$

where $\sigma'_m = (\sigma'_1 + \sigma'_3)/2$ and $\tau'_m = (\sigma'_1 - \sigma'_3)/2$. σ'_1 and σ'_3 are the maximum and minimum principal effective stresses, respectively. Ψ_f and Ψ_d are the friction and dilation angles, respectively. As shown in Figure 5, the yield function of the Mohr-Coulomb model includes six corners and a common vertex on the tension side of the hydrostatic axis. All effective stresses need to be located within or on the yield surface (i.e., No effective stress is admissible outside the yield surface).

We need to determine initial and boundary conditions for the fluid/heat flow and geomechanics problems. For fluid flow, we assign boundary conditions as follows: $P_J = \hat{P}_J$ and $X_J^{\kappa} = \hat{X}_J^{\kappa}$ (with the symbol $\hat{(\cdot)}$

indicating prescribed values, $J \equiv A, G$ and $\kappa \equiv w, m$) on the boundary of the prescribed pressure Γ_P, and $\mathbf{f}^\kappa \cdot \boldsymbol{n} = \hat{f}^\kappa$ (prescribed mass flux) on the boundary of the prescribed flow Γ_f. For well-posedness, $\Gamma_P \cap \Gamma_f = \emptyset$, and $\Gamma_P \cup \Gamma_f = \partial\Omega$. The boundary conditions for heat flow are: $T = \hat{T}$ on the prescribed temperature boundary Γ_T, and $\mathbf{f}^\theta \cdot \boldsymbol{n} = \hat{f}^\theta$ (prescribed heat flux) on the corresponding boundary Γ_θ, where $\Gamma_T \cap \Gamma_\theta = \emptyset$, and $\Gamma_T \cup \Gamma_\theta = \partial\Omega$.

For geomechanics, the boundary conditions are described as follows: $\boldsymbol{u} = \hat{\boldsymbol{u}}$ (prescribed displacement) on the prescribed displacement boundary Γ_u and $\boldsymbol{\sigma} \cdot \boldsymbol{n} = \hat{\boldsymbol{\tau}}$ (prescribed traction) on the corresponding boundary Γ_σ, where $\Gamma_u \cap \Gamma_\sigma = \emptyset$, and $\Gamma_u \cup \Gamma_\sigma = \partial\Omega$. The initial stress fields should satisfy mechanical and thermodynamic equilibriums, and be consistent with the fluid pressures, temperature, and the history of the stress-strain paths. Here, we take the initial conditions of the coupled problem as $P_J|_{t=0} = P_{J,0}$, $X_J^\kappa|_{t=0} = X_{J,0}^\kappa$ ($J \equiv A, G$, $\kappa \equiv w, m$) , $T|_{t=0} = T_0$, and $\boldsymbol{\sigma}|_{t=0} = \boldsymbol{\sigma}_0$.

3.2. Discretization and simulators

We employ the finite volume method for fluid and heat flow in spatial discretization and the backward Euler method in time discretization, widely used in reservoir simulation (Aziz and Settari, 1979). The (TOUGH)+HYDRATE simulator developed at the Lawrence Berkeley National Laboratory is based on these space and time discretizations, providing local mass and heat conservation at the element level (Moridis et al., 2008). Furthermore, when combined with geomechanics, the finite volume method for flow yields relatively stable pressure fields due to piecewise constant interpolation in pressure, contrasted with the finite element method for flow that can cause spurious pressure oscillation in consolidation problems at early times (Vermeer and Verruijt, 1981). We use the equation of state module for hydrate phase implemented in TOUGH+HYDRATE. The module has been validated through simulation tests (Moridis et al., 2008).

For geomechanics, we use the "Fast Lagrangian Analysis of Continua in 3D" (FLAC3D) geomechanics simulator. This simulator adopts the finite difference method, providing first order approximation in space (i.e., convergent scheme with the lowest-order discretization) (Itasca, 2006).

3.3. Coupling and sequential methods

The previous studies on coupled flow and geomechanics for the hydrate deposits were based on one-way coupling for fluid flow and geomechanics, where the effect from fluid flow to geomechanics was considered, while the effect from geomechanics to fluid flow was not fully considered (Rutqvist and Moridis, 2009; Rutqvist

et al., 2009, 2011). Recently, Kim et al. (2012) showed clear differences between one-way and two-way couplings for numerical test cases related to gas production from hydrate bearing sediments. According to Kim et al. (2012), when we solve the coupled problem, two-way coupling is recommended because it is more rigorous and accurate for tightly coupled flow and geomechanics than one-way coupling. Thus, employing the algorithm described in Kim et al. (2012), we apply two-way coupling between fluid flow and geomechanics to field case studies of hydrate reservoirs for more rigorous geomechanical analysis, which has not been applied to previous field case studies.

The algorithm of two-way coupling presented in Kim et al. (2012) is achieved by the fixed-stress sequential method, where we solve flow first, followed by geomechanics (Kim et al., 2011c). The fixed-stress split method involves first the solution of the coupled problem of fluid flow and heat transport (while keeping the total stress fields frozen, but allowing the strain fields to vary) to determine pressure, temperature, and saturation, followed by the solution of the geomechanical equations to determine the displacements. Kim et al. (2011c) showed that the fixed-stress split provides unconditional stability and high accuracy in numerical simulation of coupled flow and geomechanics. This method can be easily coded by constructing an interface code and introducing so-called porosity correction and porosity dependent permeability. In other words, when we take single iteration between fluid-heat flow and geomechanics (i.e., staggered (sequential non-iterative) scheme), flow and geomechanics problems are communicated through updating the porosity function and its correction (Kim et al., 2012), expressed as

$$
\begin{aligned}
\Phi^{n+1} - \Phi^{n} &= \underbrace{\left\{ \frac{b^2}{K_{dr}} + \frac{b-\Phi}{K_s} \right\}}_{\Phi c_p} \sum_{J=F} S_{J,e}^{n+1} \left(p_J^{n+1} - p_J^{n} \right) + 3\alpha_T b \left(T^{n+1} - T^{n} \right) - \Delta\Phi, \quad S_{J,e} = \frac{S_J}{\sum_{J=F} S_J}, \\
\Delta\Phi &= \frac{b^2}{K_{dr}} \sum_{J=F} S_{J,e}^{n} \left(p_J^{n} - p_J^{n-1} \right) + 3\alpha_T b \left(T^{n} - T^{n-1} \right) - b \left(\varepsilon_v^{n} - \varepsilon_v^{n-1} \right) \\
&= -\frac{b}{K_{dr}} \left(\sigma_v^{n} - \sigma_v^{n-1} \right), \qquad (17)
\end{aligned}
$$

where b is Biot's coefficient in a single fluid phase flow system (Biot, 1941). Φ is Lagrange's porosity, defined as the ratio of the pore volume in the deformed configuration to the bulk volume in the reference (initial) configuration. K_{dr} is the 3D drained bulk modulus. For elastoplasticy, K_{dr} becomes the 3D drained elastoplastic tangent bulk modulus. K_s is the intrinsic solid grain bulk modulus. p_J and S_J are pressure and saturation of the fluid phase J. $3\alpha_T$ is the coefficient of volumetric skeleton thermal dilation. T is temperature. The superscript

n $(\cdot)^n$ indicates time level. $\sum_{J=F} S_J$ is the sum of fluid phase saturation, where F implies fluid phase. σ_v is the total volumetric (mean) stress. $\Delta\Phi$ is called a porosity correction term, which sequentially corrects the inconsistency between the porosity computed from a conventional flow simulator and the strains from a mechanical simulator (Settari and Mourits, 1998; Kim et al., 2011a). c_p corresponds to a pore compressibility in the conventional reservoir simulation, and it plays a critical role in numerical stability in the coupled flow and geomechanics sequential simulation (Jean et al., 2007; Kim et al., 2011c; Mainguy and Longuemare, 2002).

When permeability is coupled to geomechanics, We can use the porosity-dependent permeability proposed by Moridis et al. (2008) in this paper, written as

$$\mathbf{k} = \mathbf{k}_0 \exp\left[\gamma_1 \left(\frac{\Phi}{\Phi_0} - 1\right)\right] \left(\frac{\Phi_a - \Phi_c}{\Phi_0 - \Phi_c}\right)^{\gamma_2}, \quad \Phi_a = \Phi(S_A + S_G), \tag{18}$$

where the subscript 0 indicates the reference state (i.e., initial state). γ_1 and γ_2 are determined experimentally. Φ_c is a critical porosity at which permeability is reduced to zero. Thus, permeability is coupled to geomechanics through the updated porosity. Alternatively, in the case of fractured reservoirs, we may employ a specific empirical relation between permeability and geomechanical variables directly, such as effective stress or total strain.

The computational efforts for one-way and two-way couplings are almost the same. The additional computational cost for two-way coupling is only the local calculation of Lagrange's porosity correction term $\Delta\Phi$, which is negligible when compared to the global computational cost. In terms of memory requirement, the two-way coupling approach necessitates the allocation of additional memory only for P_J, T, and S_J (or the volumetric (mean) total stress) at the $n-1$ time step. Since we update the porosity function, the code modification is easy and straightforward.

4. Numerical simulation

Moridis et al. (2010) investigated the performance of vertical and horizontal well production scenarios at Unit C of the PBU-L 106 site with constant well bore pressure conditions in gas production, using the depressurization method. In Moridis et al. (2010), simulation results of gas production using a single vertical well show that the gas production rate Q_p increases during the 2 year long term test, where a maximum $Q_p = 2.25 \times 10^3\ m^3/day$ and a cumulative volume of produced gas $V_p = 80 \times 10^3\ m^3$at the standard temperature condition. Such a production rate is generally low, because of the vertical well configuration and

the relatively low initial temperature and pressure at this site. On the other hand, when we use a horizontal well production scenario, Q_p and V_p increase by orders of magnitude (i.e., $Q_p = 9.0 \times 10^3\ m^3/day$ and $V_p = 5.27 \times 10^6\ m^3$). Since both production scenarios are feasible, we investigate geomechanical behavior for both vertical and horizontal well scenarios in this paper. We use the same input data for flow as used in Moridis et al. (2010), described as follows. This is a relatively generalized reservoir model, not representing all the specific details of the reservoir conditions and geometries.

4.1. Simulation domain and input data

For the vertical well, as shown in Figure 6, we have 47427 grid blocks (i.e., 247×192 in radial r and vertical z directions). The size of the domain is $2000\ m \times 753.3\ m$ in radial and vertical directions, respectively. The spacing along the vertical direction (z direction) within the hydrate layers, shale interlayer, and boundaries in the immediate vicinity of the hydrate layers is uniform ($\Delta z = 0.3\ m$), while that within the top and bottom shale layers is non-uniform and increasing near the top and bottom of the domain. Along the radial direction, the spacing is non-uniform and increasing logarithmically from the well to the boundary, where the smallest spacing nearest to the well is $0.05\ m$.

For the horizontal well, as shown in Figure 7, we have 57600 grid blocks (i.e., 300×192 in horizontal x and vertical z directions). The size of the domain is $1773m \times 753.3m$ in the horizontal and vertical directions, respectively. The vertical discretization is the same as the cylindrical system (i.e., the vertical well), while the horizontal discretization is non-uniform, increasing logarithmically from the well to the boundary, where the smallest spacing nearest to the well is $0.05\ m$.

For both wells, initial intrinsic permeability and porosity of the hydrate layers (C1 and C2) are $k_0 = 1\ \mathrm{Darcy}(9.87 \times 10^{-13}\ m^2)$ and $\Phi_0 = 0.4$, while those of the shale layers are $k_0 = 0\ \mathrm{Darcy}(0\ m^2)$ and $\Phi_0 = 0.05$, respectively. We use $\gamma_1 = 0$, $\gamma_2 = 3.0$ and $\Phi_c = 0$ for the permeability model in Equation 18. Thermal expansion is $\alpha_T = 0.0$, and Biot's coefficient is $b = 1.0$. We have a medium specific heat of $C_R = 1000\ Jkg^{-1}\ {}^oC^{-1}$, a *wet* thermal conductivity $k_{\theta w} = 3.1\ Wm^{-1}\ {}^oC^{-1}$, a *dry* thermal conductivity of $k_{\theta d} = 1.0\ Wm^{-1}{}^oC^{-1}$, and a composite thermal conductivity computed from the Moridis et al. (2005) relationship. Liquid water and hydrate saturations in C1 and C2 are $S_A = 0.25$ and $S_H = 0.75$, while those in shale layers are $S_A = 1.0$ and $S_H = 0.0$. We have no capillarity. Aqueous phase pressure and temperature are distributed from $P_A = 7.3$ MPa and $T = 5^o$C (top) to $P_A = 7.7$ MPa and $T = 6.5^o$C (bottom), respectively, as described in the previous section. The initial total stresses are distributed from surface (0.0 MPa) with vertically

-19.62 kPa/m and horizontally -15 kPa/m. We use the geomechanical properties presented in the previous section. The bulk density is $\rho_b = 2000\ kg/m^3$. No flow boundary conditions for flow are applied to all the boundaries. We use 3.0 MPa constant well bore pressure conditions for both wells. For geomechanics, we have no-horizontal displacement boundaries at both sides, no-vertical displacement boundaries at the bottom. Note that the initial effective stresses are not zero at the beginning of the simulation, which can be calculated using the initial total stress and fluid pressure (Kim et al., 2012).

4.2. Results and discussion

4.2.1. Vertical well

We first investigate the vertical well production scenario. Figures 8 and 9 show the spatial distributions of the aqueous phase pressure, total volumetric strain, temperature, and hydrate saturation at the upper and lower hydrate layers (i.e., C2 and C1), respectively, after 232 days. We observe the pressure drop around the vertical well (Figures 8 (a) and 9 (a)), the area of which corresponds to the distribution of hydrate saturation where hydrates are dissociated due to depressurization (Figures 8 (d) and 9 (d)). Then, based on thermodynamic equilibrium, the pressure drop results in the decrease of temperature (Figures 8 (c) and 9 (c)). Compaction occurs around the production well because the aqueous phase pressure drops, while dilation occurs away from the well due to the horizontally constrained boundary condition (Figures 8 (b) and 9 (b)).

Figure 10 shows evolution of the pressure at the top shale ($r = 1.45\ m$, $z = -651.44\ m$) and hydrate layers ($r = 1.45\ m$, $z = -678.63\ m$), respectively. Note that the vertical well is located from $z = -678.48\ m$ through $z = -723.68\ m$. Since the mechanical problem is quasi-static, which yields an elliptic partial differential equation, the instantaneous pressure drop by the constant well bore pressure (i.e., 3.0 MPa) causes deformation over the entire reservoir domain immediately. As shown in Figure 10 (a), we find that, when two-way coupling is used, the aqueous pressure rises initially at ($r = 1.45\ m$, $z = -651.44\ m$) in the shale layer, because there is no pressure diffusion due to the impermeable porous medium and compaction around the well (Mandel-Cryer effect). After initial time, changes in flow variables such as aqueous pressure and hydrate saturation in the hydrate layers during simulation significantly influence fields of mechanical variables such as total stress and strain over the entire domain, including the shale layer. Redistributions of the mechanical variables, in turn, change aqueous pressure during simulation at ($r = 1.45\ m$, $z = -651.44\ m$), even though the shale layer is impermeable.

On the other hand, one-way coupling cannot capture any changes in aqueous pressure because there is no

feedback from geomechanics to fluid flow in pore volume. In one-way coupling, the pressure can only change by pressure diffusion. Since the diffusivity is zero because of the impermeable layer in the shale layer, there is no change in the aqueous pressure when one-way coupling is used.

In Figure 10 (b), there is no difference between one-way and two-way couplings, because the pressure diffuses fast, and the mechanical effect from geomechanics in pore volume is negligible. Kim et al. (2012) showed the above pressure behavior in a 2D test problem of a small hydrate reservoir, explaining that the fundamental reason for differences between the two coupling methods is due to two different time scales between fluid/heat flow and geomechanics. We observe some pressure oscillations in time, as shown in Figure 10. Moridis et al. (2010) also showed oscillations in gas and water production when solving uncoupled flow problems, from which we can infer that the oscillations in Figure 10 originate from the flow simulation.

Figure 11 shows evolution of the effective stresses (σ'_m and τ'_m) corresponding to Figure 10. The analysis of the effective stresses is an important task when we evaluate geological stability. Figure 11 (a) shows that σ'_m and τ'_m at ($r = 1.45\ m$, $z = -651.44\ m$) decrease for both coupling methods. The effective stresses are still within the elastic region, located away from the Mohr-Coulomb failure line. The path of the effective stresses in two-way coupling is slightly above the path in one-way coupling. On the other hand, in Figure 11 (b), σ'_m and τ'_m at ($r = 1.45m$, $z = -651.44\ m$) increase for both coupling methods in contrast with Figure 11 (a). However, similar to Figure 11 (a), the effective stresses at ($r = 1.45\ m$, $z = -651.44\ m$) are within the elastic region, and the path of the effective stresses in two-way coupling is above the path in one-way coupling.

Figure 12 shows evolution of the effective stresses at ($r = 1.45\ m$, $z = -653.59\ m$) and ($r = 1.45\ m$, $z = -654.79\ m$), deeper than the locations of Figure 11. τ'_m at ($r = 1.45\ m$, $z = -653.59\ m$) decreases from 1.45 MPa to 1.1 MPa, and then increases to 1.35 MPa, while σ'_m decreases from -4.7 MPa to -5.6 MPa (Figure 12 (a)). The evolution of the effective stresses at ($r = 1.45\ m, z = -654.79\ m$) also shows similar behavior to Figure 12 (b), although there is some non-smooth variation in the evolution. Both figures show that the effective stresses are within the elastic region. We investigate geological stability at other locations, and find that the effective stresses do not enter the plastic region. The results also show that differences in the effective stresses between the two coupling methods are not significant, even though they are still slightly noticeable.

We investigate evolution of the vertical displacement at ($r = 0.5\ m$, $z = -678.5\ m$) and ($r = 0.5\ m$, $z = -705.3\ m$), using two-way coupling. In Figure 13 (a), the vertical displacement at ($r = 0.5\ m$, $z = -678.5\ m$) decreases to $-3.47\ cm$, whereas the vertical displacement at ($r = 0.\ 5m$, $z = -678.5\ m$) increases

to $0.95\ cm$. As shown in Figures 8 (d) and 9 (d), subsidence and uplift at the two locations correspond to compaction and dilation around the well area, respectively. At the end of simulation, the vertical displacement ranges from $-3.67\ cm$ to $3.62\ cm$ over the domain, mainly from $-2.0\ cm$ to $0.0\ cm$. This vertical displacement is not significant. Thus, in the light of evolution of the effective stresses and vertical displacement, there is little danger in stability of the production well and surface facilities. This result is in agreement with the analysis by Rutqvist et al. (2011) in one-way coupling.

4.2.2. Horizontal well

We investigate the reservoir performance in the case of the horizontal well production scenario, considering the interaction between fluid/heat flow and geomechanics. Figures 14 and 15 show spatial distributions of the aqueous phase pressure, total volumetric strain, temperature, and hydrate saturation at the upper and lower hydrate layers (i.e., C2 and C1), respectively, after 231 days. Even though the horizontal well yields the similar pressure drop and large hydrate dissociation to the previous case of the vertical well, we can obtain a large amount of gas production because of the large length of the horizontal well. Moridis et al. (2010) estimates a larger amount of hydrate dissociation and gas production using the horizontal well than the vertical well.

Physical behavior in the case of the horizontal well scenario is similar to that for the vertical well. Depressurization induces dissociation of the gas hydrates (Figures 14 (a) and (d), and 15 (a) and (d)). The decrease of the aqueous phase pressure induces the decrease of temperature due to thermodynamic equilibrium (Figures 14 (c) and 15 (c)). Fluid production results in compaction around the production well, and the area of the compaction matches the area of the aqueous pressure drop (Figures 14 (b) and 15 (b)).

Figure 16 shows evolution of the aqueous pressure at the top shale ($x = 234.1\ m$, $z = -678.33\ m$) and hydrate ($x = 234.1m$, $z = -678.63\ m$) layers. Even though the two locations are very close, we observe different evolutions in the pressure at the two locations. The top shale layer behaves as undrained geomechanics because it is impermeable, whereas the hydrate layer does as drained geomechanics due to high permeability. We observe the rise of the pressure at the top shale layer at early times due to compaction of the hydrate reservoir and the undrained condition of the shale layers, showing slight differences between one-way and two-way couplings, as shown in Figure 16 (a). On the other hand, the pressure at the hydrate layer dissipates fast due to the relatively high permeability (Figure 16 (b)), where we also observe small pressure buildup at the initial times for two way coupling based on the same physics in Figure 16 (a). The aqueous pressure values from two-way coupling are higher than those from one-way coupling, because two way coupling can account for the

pressure support induced by reservoir compaction. The reservoir compaction also decreases porosity and forms the secondary hydrates (Kim et al., 2012), causing the lower effective permeability. As a result, the pressure diffusion in two way coupling, which can detect all the above physics from the reservoir compaction, becomes lower than that in one way coupling, which cannot capture them.

We also find clear differences in the effective stresses at the two locations. In Figure 17 (a), at ($x = 234.1\ m$, $z = -678.33\ m$) in the shale layer, τ'_m increases to 1.59 MPa with little change in σ'_m, and then σ'_m increases, showing some difference between one-way and two-way couplings. On the other hand, at ($x = 234.1\ m$, $z = -678.63\ m$) in the hydrate layer, τ'_m increases to 1.63 MPa, and then σ'_m decreases, as shown in Figure 17 (b). Here, we also observe clear difference between one-way and two-way couplings. For further analysis of geological stability, we investigate evolution of the effective stresses at the upper and lower horizontal wells (Figure 18 (a) and (b), respectively). Note that the upper and lower wells are located at $z = -678.48\ m$ and $z = -704.78\ m$, respectively. Due to the instantaneous pressure drop at the wells, we observe a jump from ($\sigma'_m = -8.8$ MPa, $\tau'_m = 1.6$ MPa) to ($\sigma'_m = -5.7$ MPa, $\tau'_m = 2.2$ MPa) at both wells at initial time. After the initial jump, the effective stresses propagate to the upper and left direction. The effective stresses at the locations close to the wells ($0.54\ m$ distance from the wells in the horizontal direction) also propagate to the upper and left direction, shown in Figure 19. From Figures 18 and 19, we observe little difference in the effective stresses near the wells in the hydrate layer between the two coupling methods. On the other hand, Figure 20 shows evolution of the aqueous pressure and effective stresses at ($x = 234.1\ m$, $z = -704.73\ m$), far away from the wells, and we observe some differences between the two coupling methods. The effective stresses at the location are within the elastic region, away from the yield function, as shown in Figure 20. During simulation, all effective stresses over the domain are within the elastic region, not indicating significant geological instability. All the above observations and characteristics from the evolutions in the effective stresses are in agreement with the findings and discussions in Kim et al. (2012).

We investigate evolution of the vertical displacement at ($x = 0.\ 5m$, $z = -678.5\ m$) and ($x = 0.5\ m$, $z = -705.3\ m$), using two-way coupling. The two locations are the same as we observe for the vertical well production scenario. In Figure 21 (a), the vertical displacement at ($x = 0.5\ m$, $z = -678.5\ m$) decreases to $-16\ cm$ at the end of simulation. Compared with the vertical well scenario at the same simulation time, the vertical displacement for the horizontal well is $-9\ cm$, three times greater than that for the vertical well. On the other hand, at the same simulation time, we observe $2.2\ cm$ vertical uplift at ($x = 0.5\ m$, $z = -705.3\ m$),

which is also larger than that for the vertical well (Figure 21 (b)). We observe that the vertical displacement ranges from $-15.4\ cm$ to $5.7\ cm$ over the domain at the end of simulation.

Let us consider a simple calculation based on uniaxial reservoir compaction and single fluid phase for approximation of the vertical displacement for the horizontal well scenario (Fjaer et al., 2008), written as

$$\frac{\Delta l}{l} = \frac{b}{K_{dr}^{C}} \Delta P_{A},, \quad K_{dr}^{C} = \frac{(1+\nu)(1-2\nu)}{(1-\nu)} E, \tag{19}$$

where ν and E are Poisson's ratio and Young's modulus, respectively. This approximation can provide an estimate of the maximum vertical displacement and strain. Δl and l are the vertical displacement and reservoir thickness. K_{dr}^{C} is the drained constrained modulus and Δp_A is the total aqueous pressure drop. For the drained bulk and shear moduli used for Unit C of the PBU L 106 site, we have $K_{dr}^{C} = 211, 1167, 1486$ MPa for $S_H = 0.0, 0.75, 1.0$, respectively. Then, Δl ranges from $13\ cm$ at $S_H = 0.75$ (i.e, 0.4 % of the vertical strain) to $73\ cm$ at $S_H = 0.0$ (i.e., 2 % of the vertical strain), when we use the given bottom hole pressure, 3.0 MPa (i.e., $\Delta p_A = 4.3$ MPa), $b = 1.0$, and the total thickness of the hydrate layers, 36 m. The vertical well production has the same estimate of the vertical displacement as the horizontal well production, because this estimate is based on the case that the hydrates are completely dissociated and the aqueous phase pressure is equilibrated with the constant bottom hole pressure, independent of a type of production wells. Consequently, we might face large subsidence for long term production when hydrates become dissociated significantly over the reservoir domain, because the drained bulk and shear moduli are reduced considerably due to the hydrate dissociation. However, even though we may have relatively large subsidence due to full dissociation of the hydrates, the horizontal well production appears to be feasible, keeping the well assembly safe, because the estimate of the maximum vertical strain is about 2 %, less than 5 %. Reservoir compaction greater than 5% is a typical and consistent indicator for potential casing failure (Moridis et al., 2011). Note that the simulation results in this study are based on the generalized reservoir model that contains several assumptions such as the failure model and geomechanical properties, which are approximated from other experimental and field data (Masui et al., 2005, 2008; Rutqvist et al., 2009; Moridis et al., 2010; Rutqvist et al., 2011). Thus, a specific reservoir model for the PBU-L 106 unit C site with accurately measured geomechanical data and failure models is required for higher accuracy in geomechanical analysis.

5. Conclusions

We performed simulations for Unit C in the PBU-L 106 site, using two-way coupling for coupled flow and geomechanics, and compared results between one-way and two-way coupling methods. From the results, we have found that there are noticeable differences in the aqueous phase pressure and effective stresses between the two coupling methods. We confirmed in all the simulations that the computational cost in two-way coupling is almost the same as that in one-way coupling.

We assessed geological stability for the vertical and horizontal well production scenarios. During simulation the effective stresses over the domain are within the elastic region for both scenarios, far away from the Mohr-Coulomb yield function. Thus, we anticipate little danger in geological instability for the given geomechanical properties in this paper.

We also investigated wellbore stability from the subsidence results. The horizontal well production scenario caused larger vertical displacement for the same simulation time than the vertical well, because the horizontal well production provided higher production rates. However, when analyzing the evolution of the vertical displacement for the horizontal well scenario, we anticipate that the estimated subsidence does not seem to be a potential danger in wellbore stability.

From the results and analyses, the horizontal well production is feasible for gas production from Unit C in the PBU-L 106 site. But the reservoir model used in this study was relatively generalized. More specific simulations of coupled flow and geomechanics will be required for accurate prediction of the site in the future after we obtain and summarize all the specific details of the flow and geomechanical properties, failure models, reservoir conditions, and geometries.

Acknowledgements

This work was supported by the Assistant Secretary for Fossil Energy, Office of Natural Gas and Petroleum Technology, through the National Energy Technology Laboratory, under the U.S. Department of Energy, Contract No. DE-AC02-05CH11231. We are grateful to the two anonymous reviewers for their constructive reviews.

References

Armero F. 1999. Formulation and finite element implementation of a multiplicative model of coupled poro-plasticity at finite strains under fully saturated conditions. *Comput. Methods Appl. Mech. Engrg.* **171**: 205–241.

Aziz K. and Settari A. 1979. *Petroleum Reservoir Simulation*. London: Elsevier.

Biot M.A. 1941. General theory of three-dimensional consolidation. *J. Appl. Phys.* **12**: 155–164.

Bird K.J. and Magoon L.B. 1987. *Petroleum geology of the northern part of the Arctic National Wildlife Refuge, Northeastern Alaska*. U.S. Geological Survey Bulletin.

Boswell R., Rose K., Collett T.S., Lee M., Winters W., Lewis K.A., and Agenda W. 2011. Geologic Controls on Gas Hydrate Occurrence in the Mount Elbert Prospect, Alaska North Slope. *Marine and Petroleum Geology* **28**.

Collett T.S. 1993. Natural Gas Hydrates of the Prudhoe Bay and Kuparuk River Area, North Slope, Alaska. *Am. Assoc. Petr. Geol. B.* **77**(5): 793 – 812.

Collett T.S. 2007. Arctic Gas Hydrate Energy Assessment Studies. Arctic Energy Summit, ANCHORAGE Anchorage, AK, 15-18 Oct.

Collett T.S., Boswell R., Lee M.W., Anderson B.J., Rose K., and Lewis K.A. 2011. Evaluation of Long-Term Gas Hydrate Production Testing Locations on the Alaska North Slope. Arctic Technology Conference, Houston, TX, oTC22149.

Collett T.S., Johnson A.H., Knapp C.C., and Boswell R. AAPG Memoir 2009. Natural Gas Hydrates: A Review. In: T. Collett, A. Johnson, C. Knapp and R. Boswell, Editors. *Natural Gas Hydrates–Energy Resource Potential and Associated Hazards* **89**: 146–219.

Fjaer E., Holt R.M., Horsrud P., Raaen A.M., and Risnes R. 2008. *Petroleum Related Rock Mechanics*. Amsterdam, The Netherlands: Elsevier B.V., second edition edition.

Gutierrez M.S. and Lewis R.W. 2002. Coupling of fluid and deformation in underground formations. *Eng Mech-ASCE* **128**(7): 779–787.

Itasca 2006. FLAC3D (Fast Lagrangian Analysis of Continua in 3 Dimensions), Version 3.1. Minneapolis, Minnesota, itasca Consulting Group.

Jean L., Mainguy M., Masson R., and Vidal-Gilbert S. 2007. Accelerating the convergence of coupled geomechanical-reservoir simulations. *Int. J. Numer. Anal. Methods Geomech.* **31**: 1163–1181.

Kim J., Moridis G.J., Yang D., and Rutqvist J. 2012. Numerical Studies on Two-way Coupled Fluid Flow and Geomechanics in Hydrate Deposits. *Soc. Pet. Eng. J.* In press, SPE 141304.

Kim J., Tchelepi H.A., and Juanes R. 2011a. Stability, Accuracy, and Efficiency of Sequential Methods for Coupled Flow and Geomechanics. *Soc. Pet. Eng. J.* **16**(2): 249–262.

Kim J., Tchelepi H.A., and Juanes R. 2011b. Stability and convergence of sequential methods for coupled flow and geomechanics: Drained and undrained splits. *Comput. Methods Appl. Mech. Engrg.* **200**: 2094–2116.

Kim J., Tchelepi H.A., and Juanes R. 2011c. Stability and convergence of sequential methods for coupled flow and geomechanics: Fixed-stress and fixed-strain splits. *Comput. Methods Appl. Mech. Engrg.* **200**: 1591–1606.

Klauda J.B. and Sandler S.I. 2005. Global distribution of methane hydrate in ocean sediment. *Energy & Fuels* **19**: 459 – 470.

Kowalsky M.B. and Moridis G.J. 2007. Comparison of Kinetic and Equilibrium Reaction Models in Simulating the Behavior of Gas Hydrates in Porous Media. *J. Energy Conv. Mgmt.* **48**(6): 1850–1863 (doi: 10.1016/j.enconman.2007.01.017).

Lewis R.W., Makurat A., and Pao W.K.S. 2003. Fully coupled modelling of seabed subsidence and reservoir compaction of North Sea oil fields. *Hydrogeol J* **11**(1): 142–161.

Lewis R.W. and Schrefler B.A. 1998. *The finite element method in the static and dynamic deformation and consolidation of porous media*. Chichester, England: Wiley, 2nd edition.

Lewis R.W. and Sukirman Y. 1993. Finite element modelling for simulating the surface subsidence above a compacting hydrocarbon reservoir. *Int. J. Numer. Anal. Methods Geomech.* **18**: 619–639.

Mainguy M. and Longuemare P. 2002. Coupling fluid flow and rock mechanics: formulations of the partial coupling between reservoir and geomechanics simulators. *Oil Gas Sci. Tech.* **57**: 355–367.

Makogon M. 1987. Gas hydrates: frozen energy. *Recherche* **18**(192): 1192.

Makogon Y. 1997. *Hydrates of Hydrocarbons*. Tulsa, OK: Penn Well Publishing Co.

Masui A., Haneda H., Ogata Y., and Aoki K. 2005. The Effect of Saturation Degree of Methane Hydrate on the Shear Strength of Synthetic Methane Hydrate Sediments. International Conference on Gas Hydrates (ICGH 2005), Trondheim, Norway, 1216 Jun.

Masui A., Miyazaki K., Haneda H., Ogata Y., and Aoki K. 2008. Mechanical Characteristics of Natural and Artificial Gas Hydrate Bearing Sediments. International Conference on Gas Hydrates (ICGH 2008), Vancouver, Canada, 610 Jul.

Milkov A.V. 2005. Global estimates of hydrate-bound gas in marine sediments: How much is really out there? *Earth Science Reviews* **66**(3): 183 – 197.

Millington R.J. and Quirk J.P. 1961. Permeability of Porous Solids. *Trans. Faraday Soc.* **57**: 1200–1207.

Miyazaki K., Aoki A.M.K., Sakamoto Y., Yamaguchi T., and Okubo S. 2010a. Study on Mechanical Behavior for Methane Hydrate Sediment Based on Constant Strain-Rate Test and Unloading-Reloading Test Under Triaxial Compression. *Int. J. Offshore Polar Eng.*, (20): 256 – 264.

Miyazaki K., Masui A., Sakamoto Y., Tenma N., and Yamaguchi T. 2010b. Effect of Confining Pressure on Triaxial Compressive Properties of Artificial Methane Hydrate Bearing Sediments. Offshore Tech. Conf. (OTC 20721), Houston, TX, 36 May.

Miyazaki K., Masui A., Tenma N., Ogata Y., Aoki K., Yamaguchi T., and Sakamoto Y. 2010c. Study on Mechanical Behavior for Methane Hydrate Sediment Based on Constant Strain-Rate Test and Unloading-Reloading Test Under Triaxial Compression. *Int. J. Offshore Polar Eng.*, (20): 61 – 67.

Moridis G.J. 2003. Numerical studies of gas production from methane hydrates. *Soc. Pet. Eng. J.* **8**(4): 359–370.

Moridis G.J., Collett T.S., Boswell R., Kurihara M., Reagan M.T., Koh C., and Sloan E.D. 2009. Toward Production From Gas Hydrates: Current Status, Assessment of Resources, and Simulation-Based Evaluation of Technology and Potential. *SPE Reserv. Eval. Eng.* **12**(5): 745–771 (doi: 10.2118/114163–PA).

Moridis G.J., Collett T.S., Pooladi-Darvish M., Hancock S.H., Santamarina C., Boswell R., Kneafsey T.J., Rutqvist J., Kowalsky M.B., Reagan M.T., Sloan E.D., Sum A., and Koh C. 2011. Challenges, Uncertainties, and Issues Facing Gas Production From Gas-Hydrate Deposits. *SPE Reserv. Eval. Eng.* **14**(1): 76–112.

Moridis G.J., Kowalsky M.B., and Pruess K. 2008. TOUGH+HYDRATE v1.0 User's Manual: A Code for the Simulation of System Behavior in Hydrate-Bearing Geologic Media. Report LBNL-00149E, Lawrence Berkeley National Laboratory, Berkeley, CA.

Moridis G.J., Reagan M., Boyle K., and Zhang K. 2010. Evaluation of a Deposit in the Vicinity of the PBU L-106 Site, North Slope, Alaska, for a Potential Long-Term Test of Gas Production from Hydrates. SPE Western Regional Meeting (SPE 133601), Anaheim, CA, 2729 May.

Moridis G.J., Seol Y., and Kneafsey T. 2005. Studies of Reaction Kinetics of Methane Hydrate Dissociation in Porous Media. The 5th International Conference on Gas Hydrates, Trondheim, Norway, lBNL-57298.

Rutqvist J., Moridis G., Grover T., and Collett T.S. 2009. Geomechanical Response of Permafrost-associated Hydrate Deposits to Depressurization-induced Gas Production. *J. Pet. Sci. Eng.* **67**: 1–12.

Rutqvist J. and Moridis G.J. 2009. Numerical Studies on the Geomechanical Stability of Hydrate-Bearing Sediments. *Soc. Pet. Eng. J.* **14**(2): 267–282.

Rutqvist J., Moridis G.J., Kim J., and Reagan M. 2011. Geomechanical Performance Analysis of Potential Long-Term Test of Gas Production from Hydrate Deposits in North Slope, Alaska. Arctic Tech. Conf. (OTC 22154), Houston, TX, 79 Feb.

Settari A. and Mourits F. 1998. A coupled reservoir and geomechanical simulation system. *Soc. Pet. Eng. J.* **3**: 219–226.

Sloan E.D. and Koh C. 2008. *Clathrate Hydrates of Nautral Gases*. Boca Raton, FL.: Taylor and Francis,.

Vermeer P.A. and Verruijt A. 1981. An accuracy condition for consolidation by finite elements. *Int. J. Numer. Anal. Methods Geomech.* **5**: 1–14.

Winters W., Dallimore S.R., Collett T.S., Katsube T.J., Jenner K.A., Cranston R.E., Wright J.F., Nixon F.M., and Uchida T. 1999. Physical Properties of Sediments for the JAPEX/JNOC/GSC. Mallik 2L-38 Gas Hydrate Research Well. Bull. - Geol. Surv. Can. 544.

Winters W.J., Waite W.F., and Mason D.H. 2008. Methane Gas Hydrate Effect on Sediment Acoustic and Strength Properties. *J. Pet. Sci. Eng.* **56**: 127 – 135.

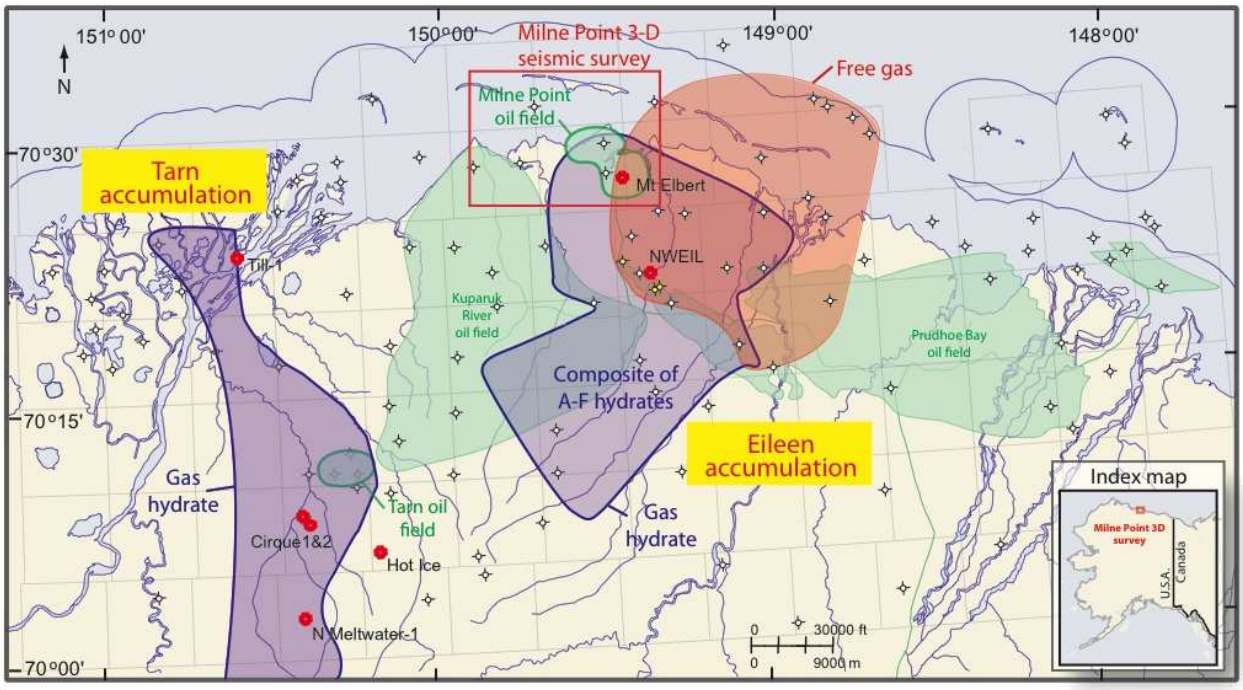

Figure 1: Regional Map of the Eileen and Tarn gas hydrate accumulations overlying portions of the Prudhoe Bay, Kuparuk River, and Milne Point oil fields in Alaska (Collett, 1993; Collett et al., AAPG Memoir 2009). The map also shows the locations of the Northwest Eileen State-2 (NWEIL) and Mount Elbert gas hydrate research wells. The PBU-L 106 site is located around NWEIL.

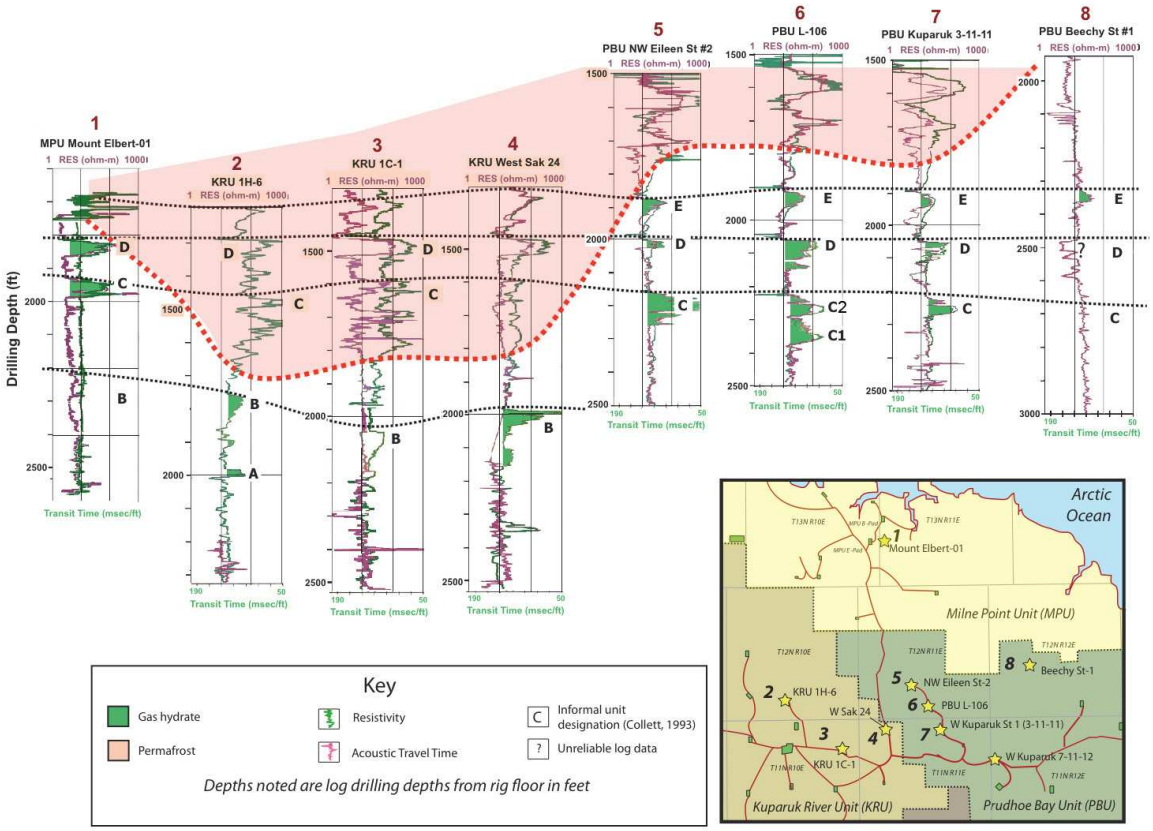

Figure 2: Cross section showing correlations of gas hydrate-bearing formations in the Prudhoe Bay-Kuparuk River area based on drill log data. This figure comes from Boswell et al. (2011). The red dotted line indicates the base of ice-bearing permafrost. The gas-hydrate-bearing units are identified with the reference letters A through E (Collett, 1993). From the logging data of Number 6 that denotes the PBU-L-106 site, Unit C of the PBU-L-106 site consists of two separate hydrate-bearing layers: C1 (deeper) and C2 (shallower).

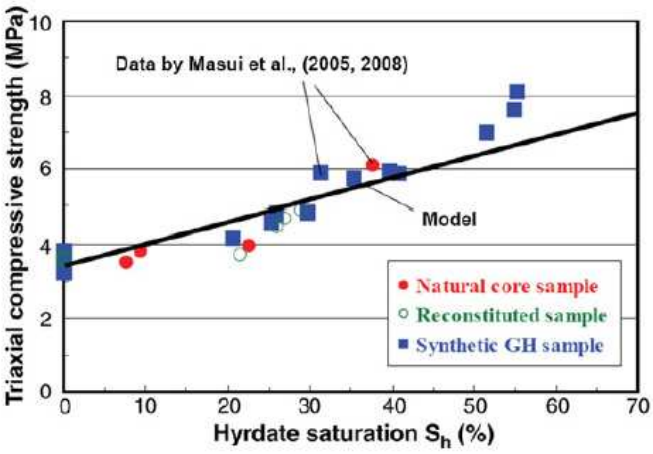

Figure 3: Laboratory data of triaxial compressive strength of artificial and natural samples of hydrate-bearing sand (Masui et al., 2005, 2008). The strength is almost linearly dependent of the hydrate saturation.

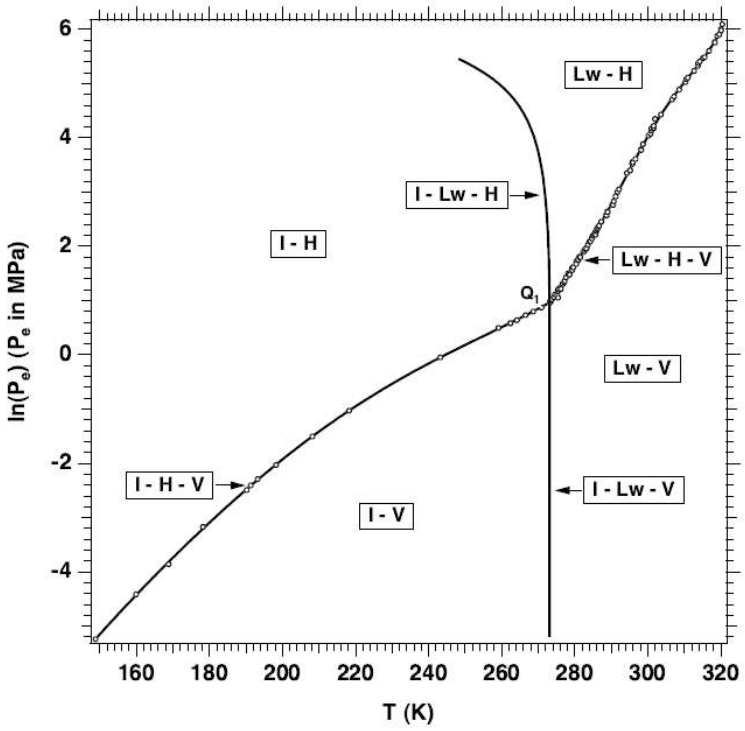

Figure 4: Pressure-temperature equilibrium relationship in the phase diagram of the water-methane-vapor-hydrate system (Moridis et al., 2008). I, V, Lw, and H indicate ice, vapor, liquid water, and hydrate phases, respectively. The dash symbol $(\cdot) - (\cdot)$ signifies coexistence of the phases. For example, $\mathrm{I} - \mathrm{H}$ means that ice and hydrate phases coexist.

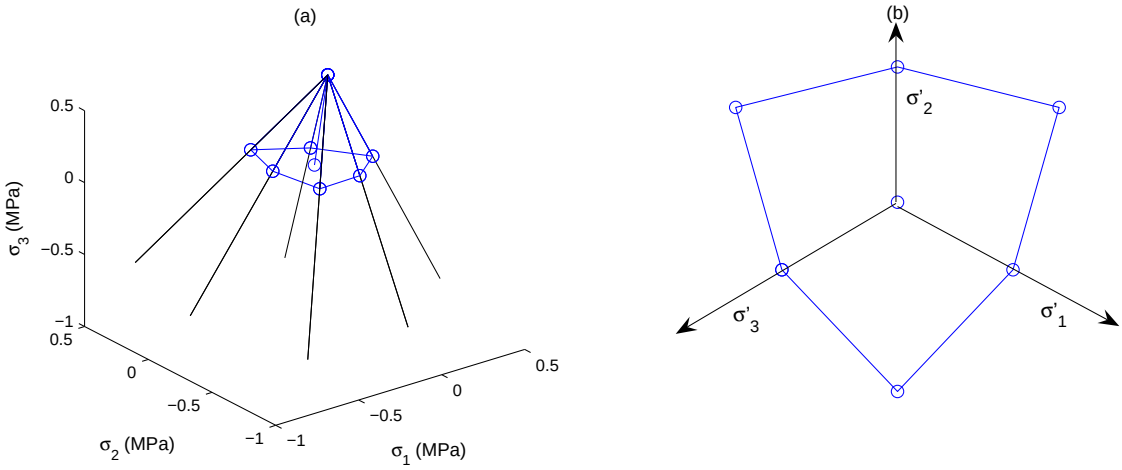

Figure 5: Mohr-Coulomb yield surface on (a) the principle effective stress space, and (b) on the deviatoric plane. σ'_1, σ'_2, and σ'_3 are the principal effective stresses. All the effective stresses are located inside the yield surface.

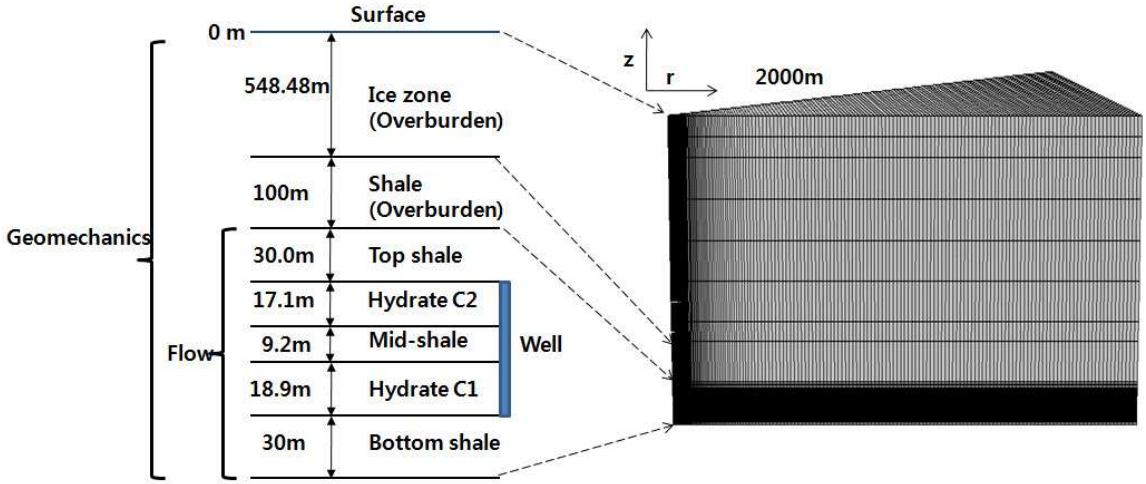

Figure 6: Domain description for the vertical well production scenario. The size of the domain is $2000m \times 753.3m$ in radial and vertical directions, respectively, with 47427 grid blocks.

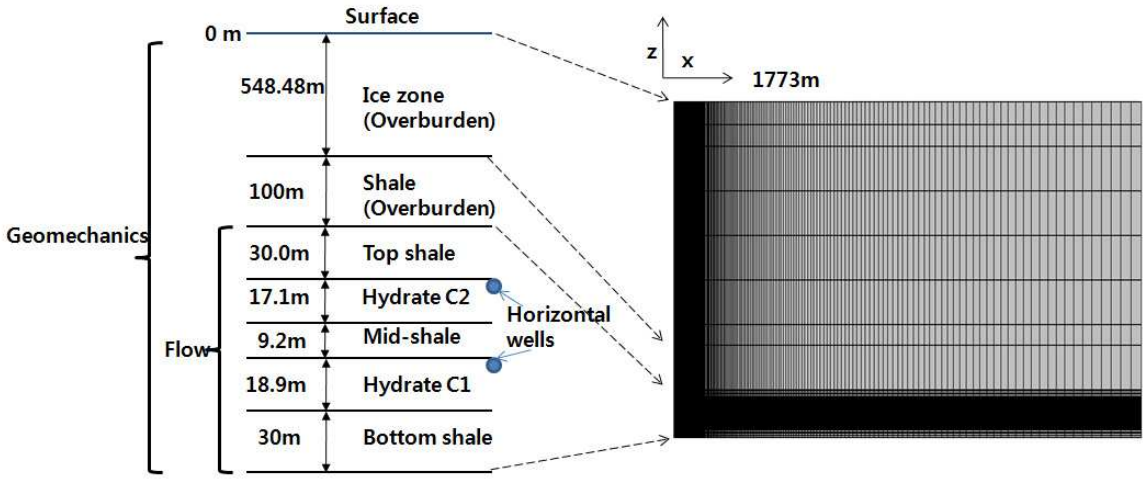

Figure 7: Domain description for the horizontal well production scenario. The size of the domain is $1773m \times 753.3m$ in horizontal and vertical directions, respectively, with 57600 grid blocks.

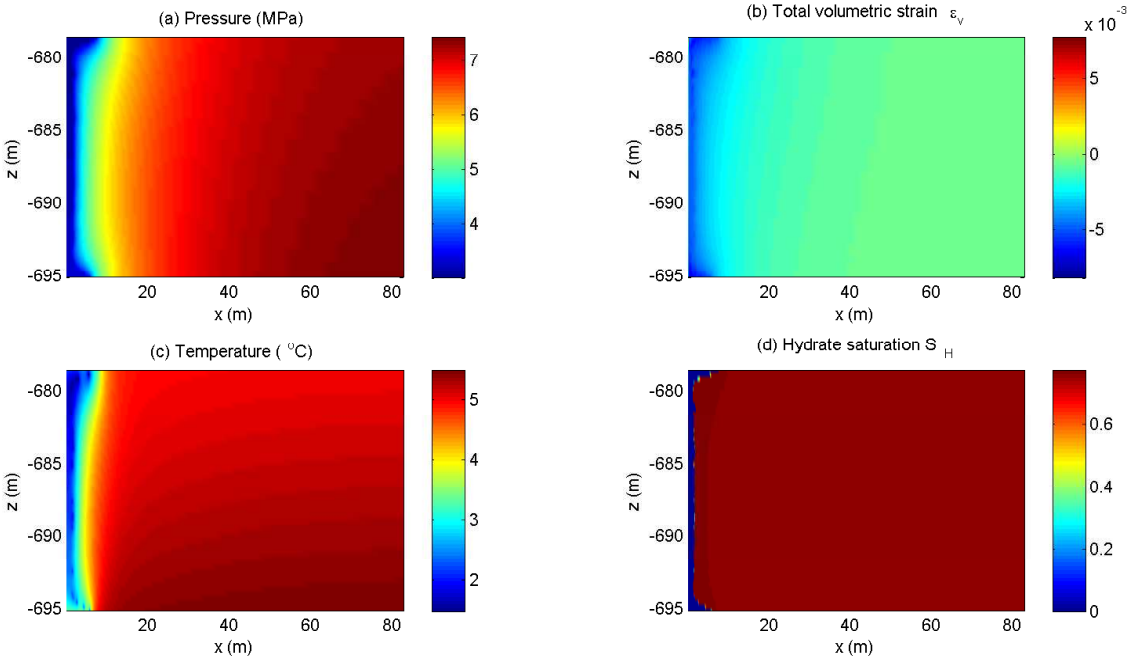

Figure 8: Spatial distributions of the aqueous phase pressure (a), total volumetric strain ε_v (b), temperature (c), and hydrate saturation (d) at the upper hydrate layer (C2) for the vertical well after 232 days. Pressure drops around the vertical well, which induces the decrease of the hydrate saturation and temperature. Depressurization also results in compaction around the well area.

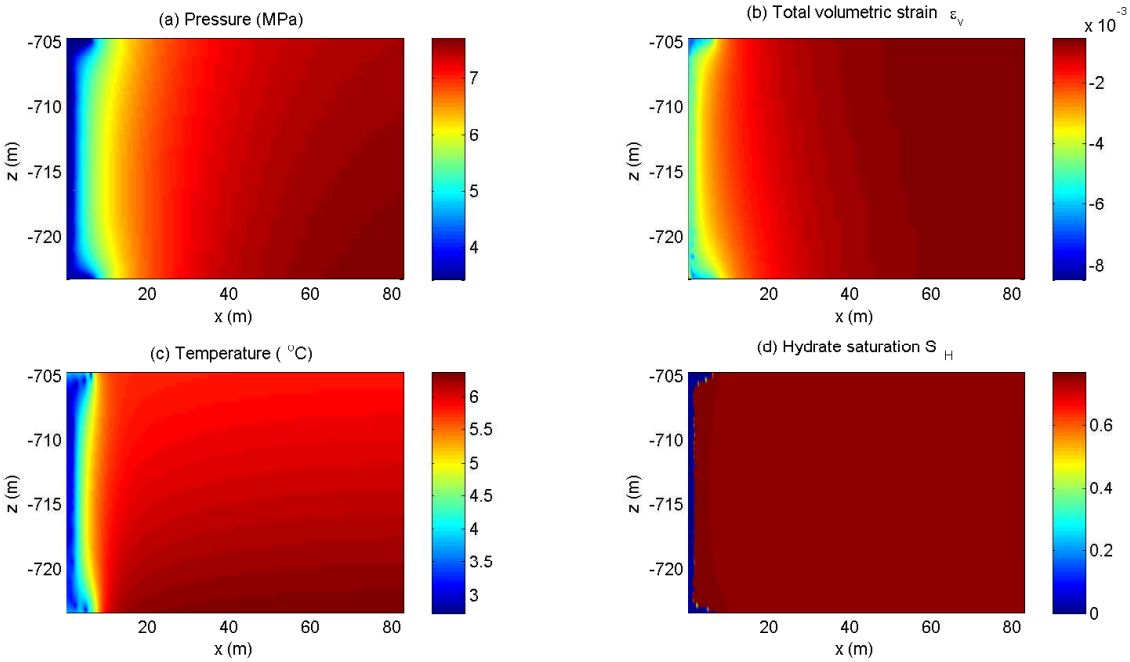

Figure 9: Spatial distributions of the aqueous phase pressure (a), total volumetric strain ε_v (b), temperature (c), and hydrate saturation (d) at the lower hydrate layer (C1) for the vertical well after 232 days. Physical behavior in C1 is similar to that in C2.

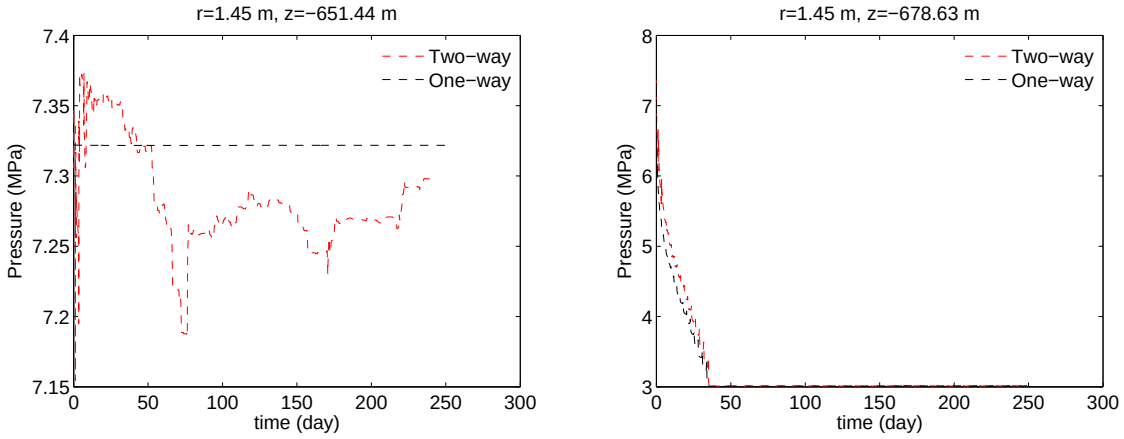

Figure 10: Evolution of the aqueous phase pressure at the top shale ($r = 1.45\ m$, $z = -651.44m$) (left figure) and hydrate layers ($r = 1.45\ m$, $z = -678.63\ m$) (right figure), respectively. Pressure rises at early time due to compaction at the shale layer, which can be captured by two-way coupling, but not by one-way coupling.

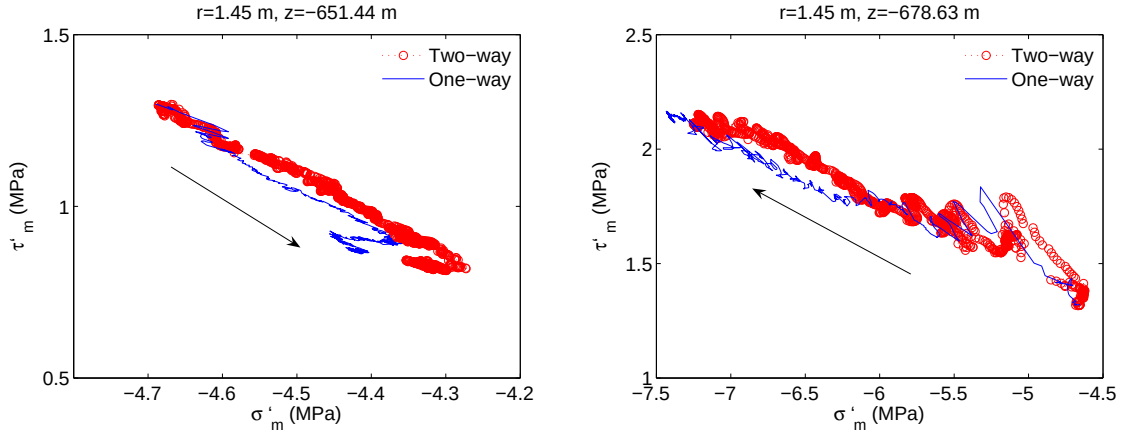

Figure 11: Evolution of the effective stresses (σ'_m and τ'_m) at ($r = 1.45\ m$, $z = -651.44\ m$) (left figure) and ($r = 1.45\ m$, $z = -678.63\ m$) (right figure), respectively. The effective stresses are within the elastic region.

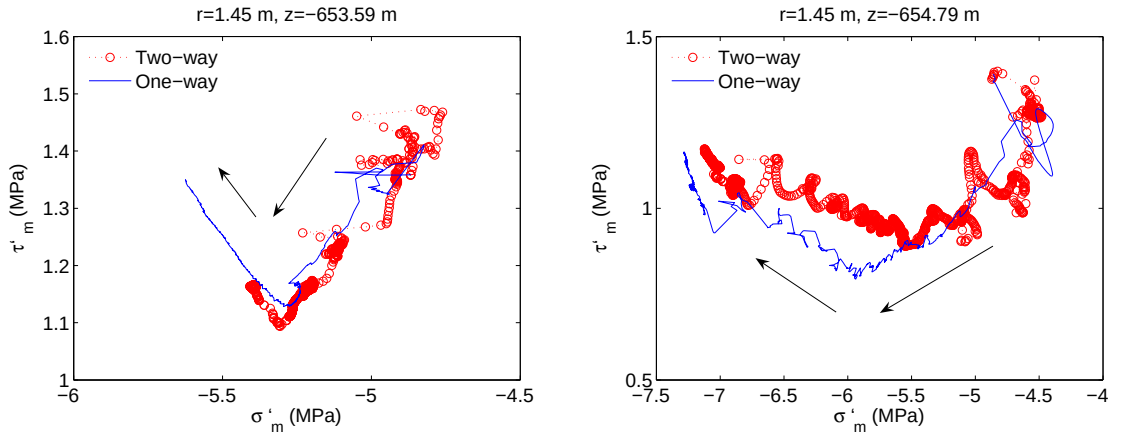

Figure 12: Evolution of the effective stresses at ($r = 1.45\ m$, $z = -653.59\ m$) (left figure) and ($r = 1.45\ m$, $z = -654.79\ m$) (right figure). The effective stresses are within the elastic region.

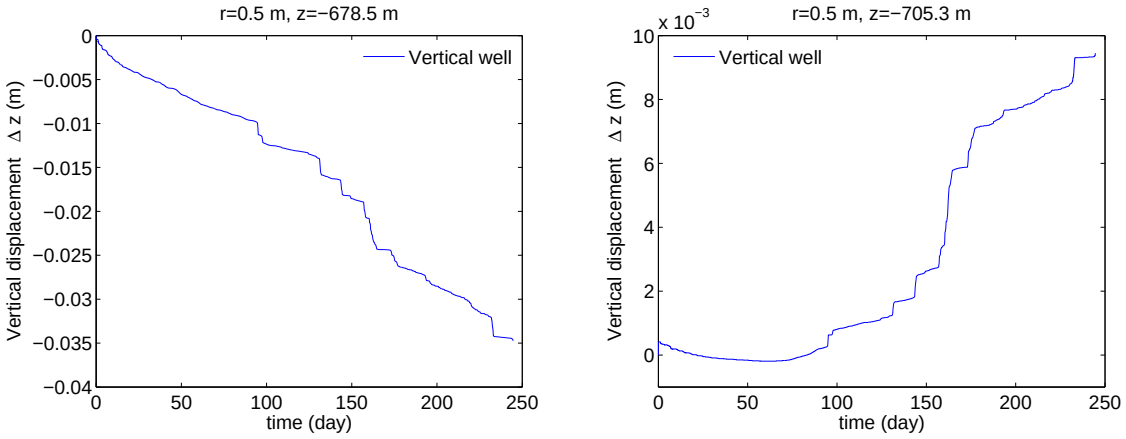

Figure 13: Vertical displacement at ($r = 0.5\ m$, $z = -678.5\ m$) (left figure) and ($r = 0.5\ m$, $z = -705.3\ m$) (right figure) for the vertical well, using two-way coupling. The vertical displacement at ($r = 0.5\ m$, $z = -678.5\ m$) decreases to $-3.47\ cm$, whereas the vertical displacement at ($r = 0.5\ m$, $z = -678.5\ m$) increases to $0.95\ cm$.

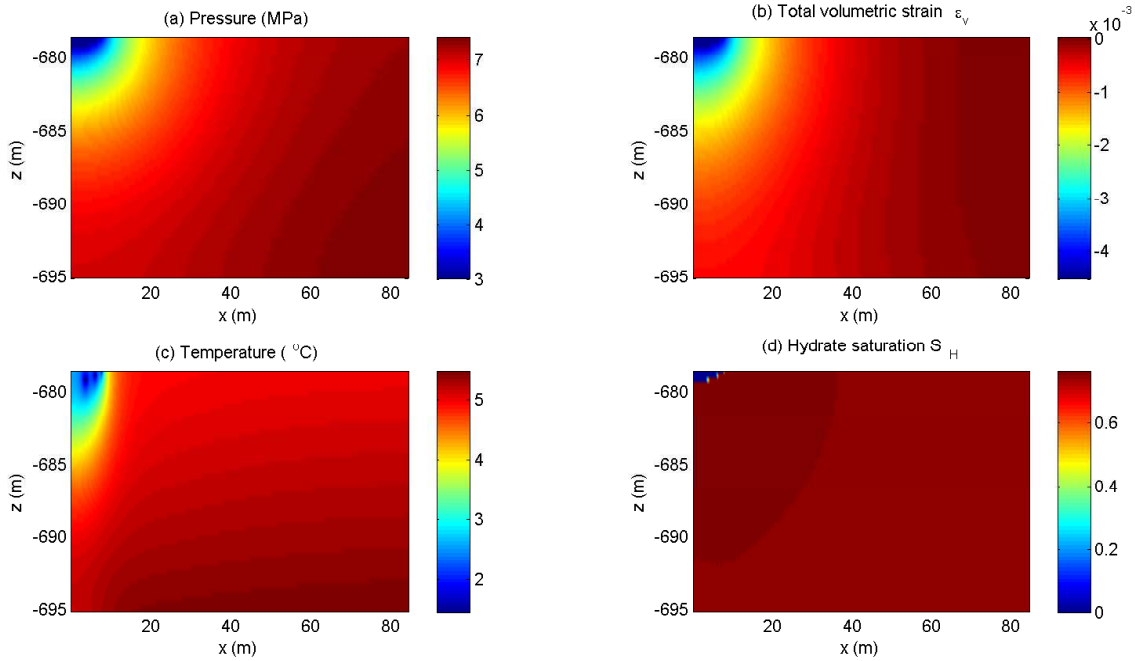

Figure 14: Spatial distributions of the aqueous phase pressure (a), total volumetric strain ε_v (b), temperature (c), and hydrate saturation (d) at the upper hydrate layer (C2) after 231 days for the horizontal well production scenario.

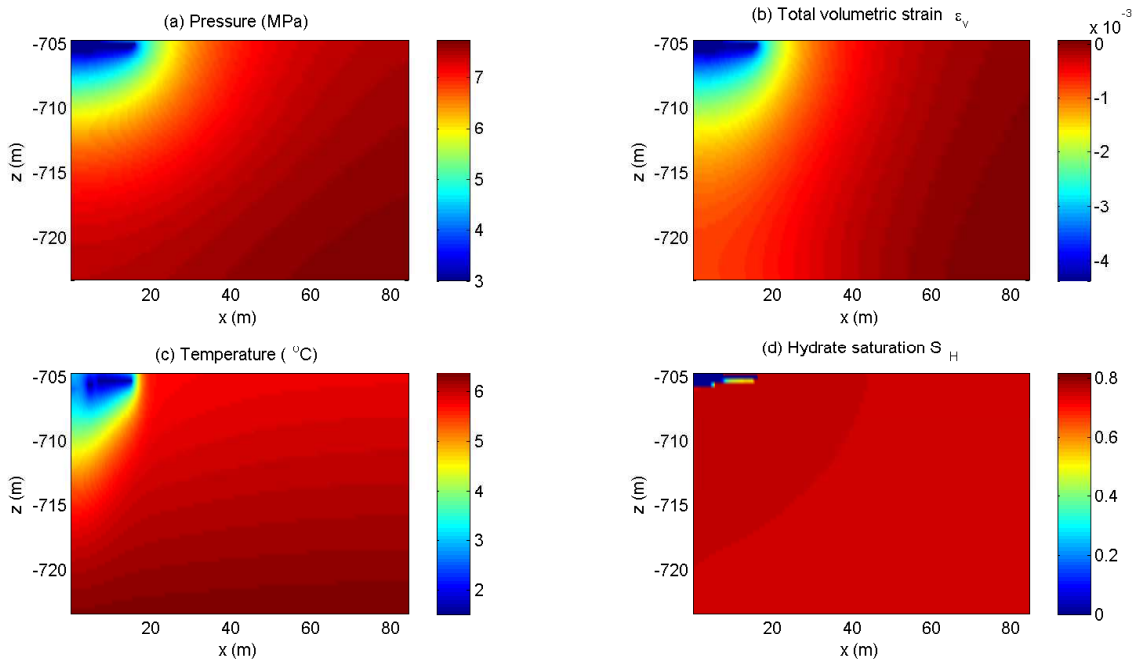

Figure 15: Spatial distributions of the aqueous phase pressure (a), total volumetric strain ε_v (b), temperature (c), and hydrate saturation (d) at the lower hydrate layer (C1) after 231 days for the horizontal well production scenario.

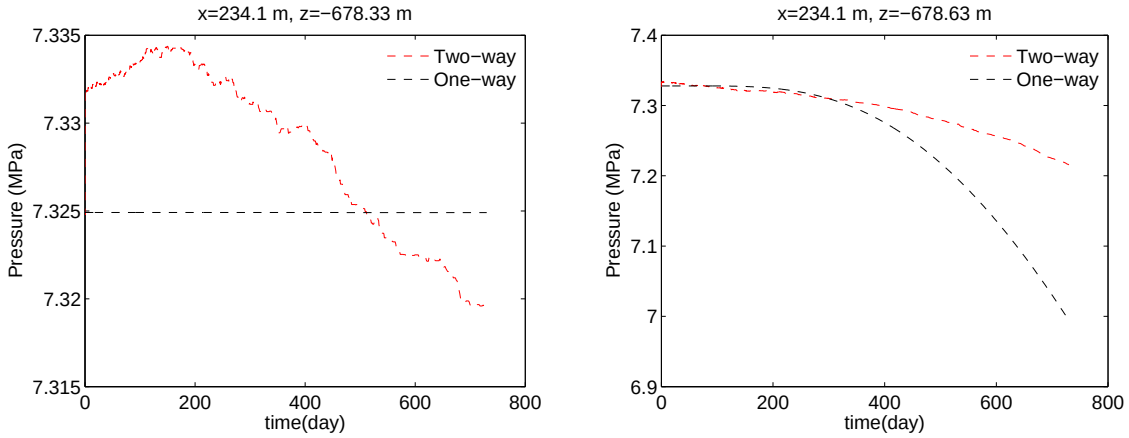

Figure 16: Evolution of the aqueous phase pressure at the top shale ($x = 234.1\ m$, $z = -678.33\ m$) (left figure) and hydrate ($x = 234.1\ m$, $z = -678.63\ m$) (right figure) layers. Pressure in the top shale layer rises at early time due to compaction of the reservoir and the undrained condition, showing significant differences between one-way and two-way couplings.

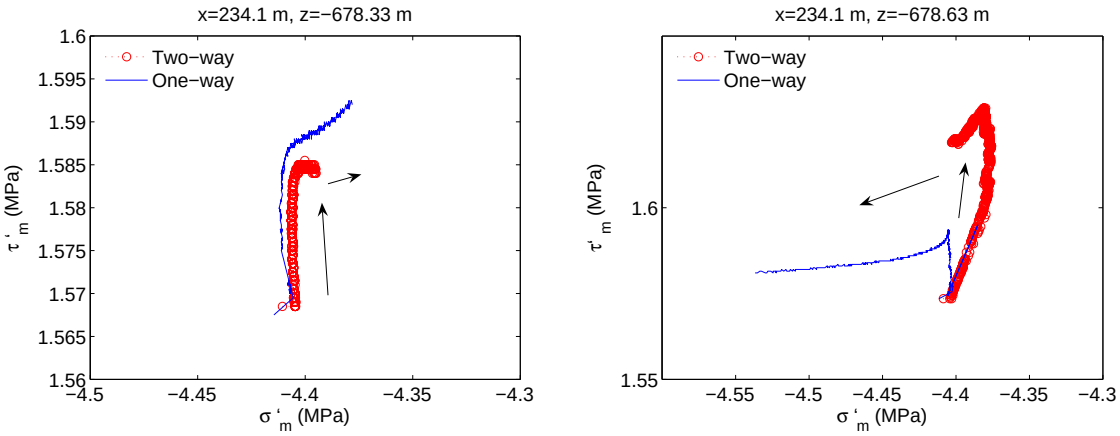

Figure 17: Evolution of the effective stresses at ($x = 234.1\ m$, $z = -678.33\ m$) in the shale layer (left figure) and at ($x = 234.1\ m$, $z = -678.63\ m$) in the hydrate layer (C2) (right figure). There are differences in the effective stresses between two coupling methods.

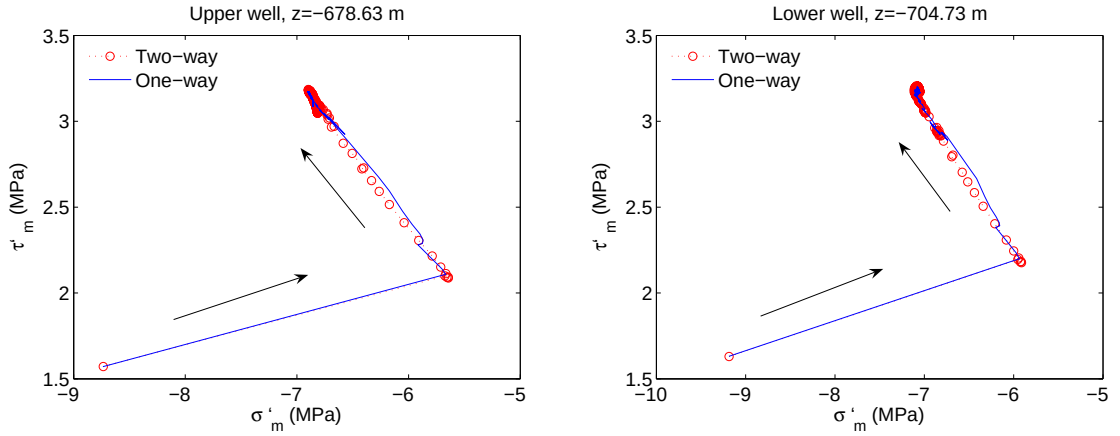

Figure 18: Evolution of the effective stresses at the upper (left figure) and lower (right figure) wells (i.e., $z = -678.63\ m$ and $z = -704.73\ m$, respectively). We find an initial jump of the effective stresses due to the instantaneous pressure drop.

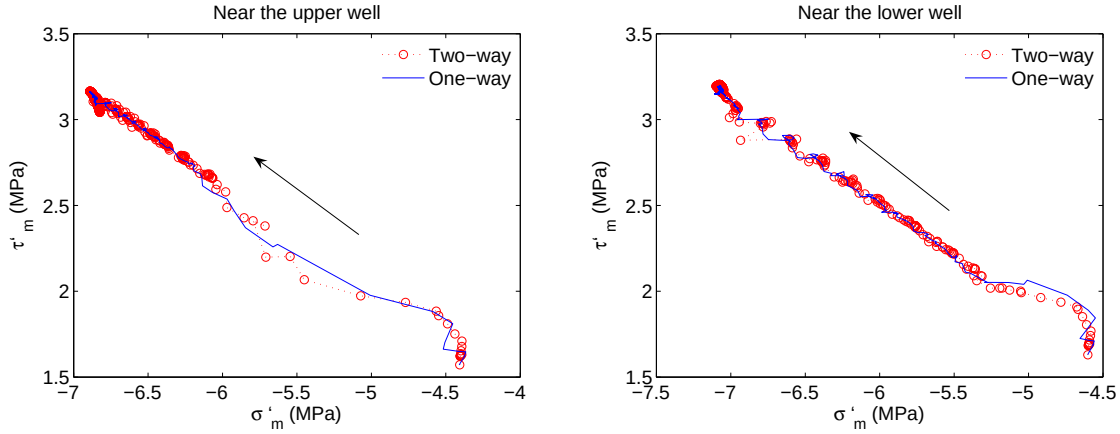

Figure 19: Evolution of the effective stresses at locations close to the upper (left figure) and lower (right figure) horizontal wells ($0.54\ m$ distance from the wells in the horizontal direction). There are little differences near the wells in the hydrate layers for the two coupling methods.

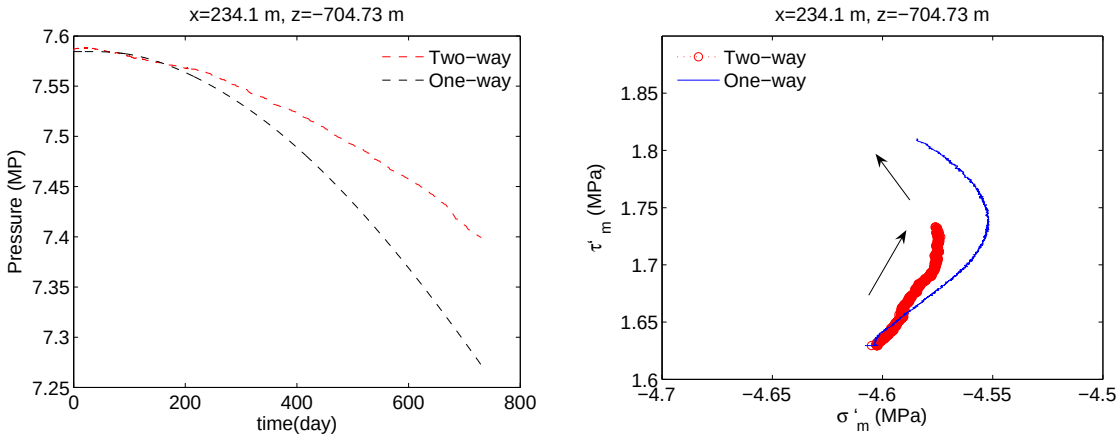

Figure 20: Evolution of the aqueous phase pressure (left figure) and effective stresses (right figure) at ($x = 234.1\ m$, $z = -704.73\ m$) in the hydrate layer (C1). There are clear differences between the two coupling methods.

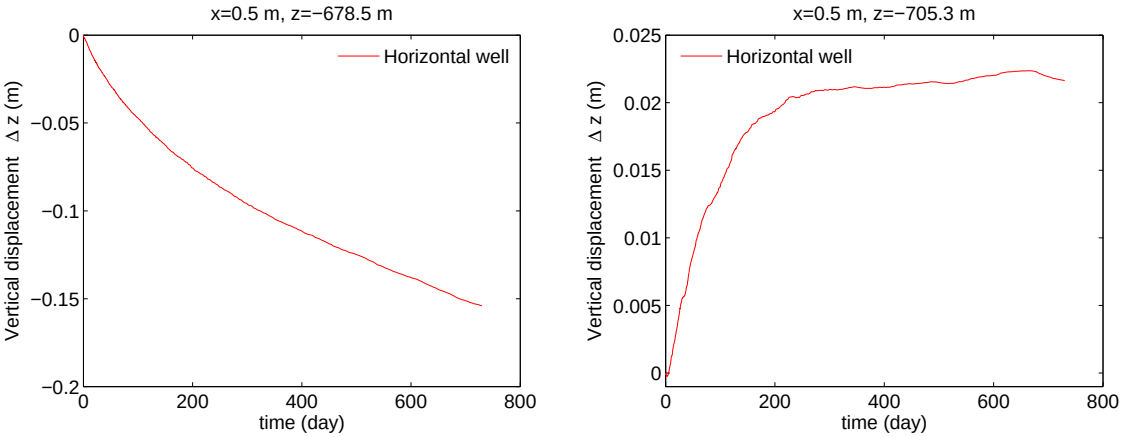

Figure 21: Vertical displacements at ($x = 0.5\ m$, $z = -678.5\ m$) (left figure) and ($x = 0.5\ m$, $z = -705.3\ m$) (right figure) for the horizontal well production scenario, using two-way coupling. The vertical displacement at ($x = 0.5\ m$, $z = -678.5\ m$) decreases to $-16\ cm$, whereas the vertical displacement at ($x = 0.5\ m$, $z = -678.5\ m$) increases to $22\ cm$.